ACS APPLIED MATERIALS & INTERFACES

Research Article

www.acsami.org

Vapor Phase Processing of α-Fe_2O_3 Photoelectrodes for Water Splitting: An Insight into the Structure/Property Interplay

Michael E. A Warwick,[†] Kimmo Kaunisto,[‡] Davide Barreca,*[,§] Giorgio Carraro,[†] Alberto Gasparotto,[†] Chiara Maccato,[†] Elza Bontempi,[∥] Cinzia Sada,[⊥] Tero-Petri Ruoko,[‡] Stuart Turner,[#] and Gustaaf Van Tendeloo[#]

[†]Department of Chemistry, Padova University and INSTM, 35131 Padova, Italy

[‡]Department of Chemistry and Bioengineering, Tampere University of Technology, 33101 Tampere, Finland

[§]CNR-IENI, Department of Chemistry, Padova University and INSTM, 35131 Padova, Italy

[∥]Chemistry for Technologies Laboratory, University of Brescia, 25123 Brescia, Italy

[⊥]Department of Physics and Astronomy, Padova University, 35131 Padova, Italy

[#]EMAT, University of Antwerp, 2020 Antwerpen, Belgium

Supporting Information

ABSTRACT: Harvesting radiant energy to trigger water photoelectrolysis and produce clean hydrogen is receiving increasing attention in the search of alternative energy resources. In this regard, hematite (α-Fe_2O_3) nanostructures with controlled nano-organization have been fabricated and investigated for use as anodes in photoelectrochemical (PEC) cells. The target systems have been grown on conductive substrates by plasma enhanced-chemical vapor deposition (PE-CVD) and subjected to eventual ex situ annealing in air to further tailor their structure and properties. A detailed multitechnique approach has enabled to elucidate the interrelations between system characteristics and the generated photocurrent. The present α-Fe_2O_3 systems are characterized by a high purity and hierarchical morphologies consisting of nanopyramids/organized dendrites, offering a high contact area with the electrolyte. PEC data reveal a dramatic response enhancement upon thermal treatment, related to a more efficient electron transfer. The reasons underlying such a phenomenon are elucidated and discussed by transient absorption spectroscopy (TAS) studies of photogenerated charge carrier kinetics, investigated on different time scales for the first time on PE-CVD Fe_2O_3 nanostructures.

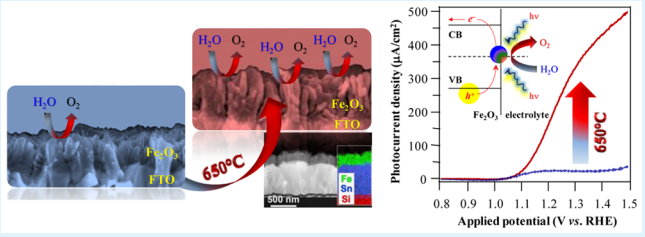

KEYWORDS: *hematite, PE-CVD, hierarchical structures, water splitting, PEC, transient absorption spectroscopy*

INTRODUCTION

The conversion of solar energy into hydrogen by means of photoelectrochemical water splitting is emerging as a sustainable area to meet global energy demands in a carbon-neutral fashion.[1−11] This strategy offers an amenable option to yield pure hydrogen, a clean and storable energy carrier that, in turn, can be converted into electrical power, becoming a key tool of the future world energy economy.[12−18] So far, numerous inorganic semiconductors (e.g., WO_3, TiO_2, $BiVO_4$, ...) have been fabricated toward the goal of producing a high-efficiency PEC system for H_2 generation.[3−7,10,15−17,19−21] Compared with other metal oxides, α-Fe_2O_3 (hematite), the most stable phase of iron(III) oxide at room temperature, is one of the most promising candidates for the development of Vis-light absorbing photoanodes.[14,22−27] Beyond the favorable band gap (E_G = 2.1 eV),[20,23,28−34] its main advantages are in fact its abundance, low cost, nontoxicity, and high chemical stability,[33,35] also in alkaline environment.[1,4,13,20,36] Nevertheless, these benefits are eclipsed by the slow reaction kinetics,[5,18,37] poor charge transport properties,[7,17] and short hole diffusion length,[9,21,30,31,34] along with comparatively long light penetration depths.[2,12,19,29] Overall, these phenomena result in an ultrafast electron−hole recombination in a ps time scale, followed by electron trapping in a ps to μs time scale and bulk recombination in a μs to ms time scale.[2,38−41] On the other hand, water oxidation has been shown to occur in a subsecond−second scale,[15,42] making imperative the need of longer carrier lifetimes to effectively drive the overall process.[6,30]

To circumvent these drawbacks and promote increased functional performances, various synthesis and modification strategies have been adopted.[11,18,35,43,44] The main ones involve doping/functionalization of α-Fe_2O_3 with suitable systems[1,5,20,24,31,37] in order to increase Vis light absorption and/or promote oxygen evolution,[2,4,6,27,30] or appropriate nanoarchitecture designing,[21,29,36,45,46] to decrease recombina-

Received: January 31, 2015
Accepted: April 8, 2015
Published: April 8, 2015

DOI: 10.1021/acsami.5b00919
ACS Appl. Mater. Interfaces 2015, 7, 8667−8676

Table 1. Processing Conditions and Relevant Material Properties for the Target Fe_2O_3 Nanodeposits[a]

sample ID	T_{dep} (°C)	T_{ann} (°C)	$I_{(110)}/I_{(012)}$	d (nm)	E_G (eV)	α^{-1} (nm)	j (μA cm^{-2})
300	300		2.4	270 ± 20	2.10	125	25
400	400		3.4	270 ± 30	2.02	85	50
300_A	300	650	4.9	380 ± 40	2.00	70	215
400_A	400	650	5.4	350 ± 50	1.93	65	240

[a]In all cases, thermal treatments were carried out in air for 1 h (heating rate = 20 °C min^{-1}). For comparison, the $I_{(110)}/I_{(012)}$ ratio calculated for the hematite powder diffractogram is 2.3.[56] T_{dep} = deposition temperature; T_{ann} = annealing temperature; d = deposit thickness; E_G = optical band gap; α^{-1} = optical penetration depth; j = photocurrent density.

tion losses.[22,34,47] In particular, nanostructured photoelectrode architectures have begun to address hematite limitations by decoupling light absorption and charge carrier extraction.[1,7,16,31] Representative examples span from nanotubes, to nanoplatelets and dendritic structures,[2,12,14,18,21,25,30] resulting in a higher contact area with the electrolyte[6−8,30] and increasing the number of holes available for H_2O oxidation, minimizing recombination processes.[1,2,5,12,23,46]

While great strides have been taken to improve the performance and understanding of H_2O oxidation with hematite electrodes, there are still several issues which need to be better understood.[4,17] In fact, many studies have been devoted to the use of wet chemical/colloidal routes, hardly enabling a simultaneous control of morphology and doping level and resulting in poor carrier collection and transport.[21,29,43] To overcome these disadvantages and obtain improved PEC performances, ex situ thermal treatments have been used by various investigators.[4,5,7,10,12−14,16,18,20,21,23,36] Nevertheless, the actual influence of annealing on the system functional behavior is often speculated but not demonstrated by pertaining experimental data. Indeed, a detailed study of photogenerated charge carrier dynamics as a function of thermal processing conditions is, so far, still missing and undoubtedly deserves further attention[16] for both fundamental and applicative purposes.

Recently, we have reported on the PEC water splitting properties of F-doped Fe_2O_3 systems supported on ITO (indium tin oxide) based on the β (bixbyite) polymorph, a scarcely investigated iron(III) oxide phase.[46] This study evidenced that the system photoefficiency was significantly influenced by the adopted growth conditions, but further issues to be addressed concern the improvement of functional performances, suppressing charge carrier recombination, and improving Fe_2O_3 catalytic activity in water splitting.

With this background in mind, in this work we report on hematite (α-Fe_2O_3) nanostructures with a hierarchical morphology for use as PEC cell photoanodes. The target systems have been obtained by PE-CVD on fluorine-doped tin oxide (FTO) substrates and subsequently subjected to annealing in air in an attempt to improve their functional performances. So far, various investigators have reported on iron(III) oxide photoanodes obtained by atmospheric pressure-chemical vapor deposition (AP-CVD),[2,34,48−51] whereas only three studies have been devoted to the PE-CVD of hematite for PEC applications[8,9,12] in spite of the great potential and industrial scalability of this technique.[52]

In this paper, the interrelations between the material chemicophysical properties and the processing conditions are investigated in detail by a number of complementary techniques. Finally, the PEC performances of the target nanomaterials are elucidated by means of TAS that enables a direct monitoring of photogenerated charge carrier dynamics during PEC water oxidation.[2,15,26,53,54] To the best of our knowledge, such analyses are performed for the first time on PE-CVD Fe_2O_3 nanomaterials as a function of the processing temperature.

EXPERIMENTAL SECTION

Synthesis. Fe_2O_3 nanomaterials were grown via PE-CVD on conductive FTO-coated glass slides (Aldrich, 735167-1EA, ≈ 7 Ω/sq; lateral dimensions = 2.0 cm × 1.0 cm; FTO thickness ≈ 600 nm), cleaned prior to each deposition by a previously reported procedure.[46,52] On the basis of preliminary optimization experiments, growth processes were performed at substrate temperatures of 300 and 400 °C for a total duration of 1 h (total pressure = 1.0 mbar; RF power = 10 W). The obtained samples were characterized both as-grown and after ex situ thermal treatments in air at 650 °C for 1 h, selected as an optimal temperature basing on previous studies.[21] In the following, specimens will be labeled according to Table 1 as a function of their growth temperature and annealing conditions. Further details on the instrumental apparatus and the adopted synthesis conditions are reported in the Supporting Information (SI).

Characterization. X-ray diffraction (XRD) measurements were carried out operating in reflection mode by means of a Dymax-RAPID microdiffractometer equipped with a cylindrical imaging plate detector, allowing data collection from 0 to 160° (2θ) horizontally and from −45 to +45° (2θ) vertically upon using Cu Kα radiation (λ = 1.54056 Å). Each pattern was collected with an exposure time of 40 min, using a collimator diameter of 300 μm. Conventional XRD patterns were then obtained by integration of 2D images.

X-ray photoelectron spectroscopy (XPS) analyses were conducted on a PerkinElmer Φ 5600ci apparatus with a standard Al Kα radiation ($h\nu$ = 1486.6 eV) at pressures <10^{-8} mbar. Charge correction was performed by assigning to the adventitious C1s signal a binding energy (BE) of 284.8 eV.[55] After a Shirley-type background subtraction, atomic percentages (at. %) were calculated by signal integration using standard PHI V5.4A sensitivity factors. Ar^+ sputtering was carried out at 4.0 kV, with an argon partial pressure of ≈5 × 10^{-8} mbar.

Secondary ion mass spectrometry (SIMS) investigation was carried out by means of a IMS 4f mass spectrometer (Cameca) using a Cs^+ primary beam (voltage = 14.5 keV; current = 25 nA; stability = 0.2%) and negative secondary ion detection, adopting an electron gun for charge compensation. Beam blanking mode and high mass resolution configuration were adopted. Signals were recorded rastering over a 150 × 150 μm^2 area and detecting secondary ions from a subregion close to 10 × 10 μm^2 to avoid crater effects.

Atomic force microscopy (AFM) analyses were carried out using a NT-MDT SPM Solver P47H-PRO instrument operating in semi-contact/tapping mode and in air. After plane fitting, root-mean-square (RMS) roughness values were obtained from 3 × 3 μm^2 images.

The system nano-organization was further characterized by field emission-scanning electron microscopy (FE-SEM) through a Zeiss SUPRA 40 VP instrument, operating at primary beam acceleration voltages comprised between 5.0 and 10.0 kV. Thickness values (Table 1) were obtained from the statistical analysis of cross-sectional micrographs.

Optical absorption spectra were recorded in transmission mode at normal incidence by a Cary 50 spectrophotometer, using bare FTO

DOI: 10.1021/acsami.5b00919
ACS Appl. Mater. Interfaces 2015, 7, 8667−8676

glass as a reference. In all cases, the substrate contribution was subtracted.

PEC measurements (see also SI for further details) were carried out in a three-electrode cell, with hematite nanodeposits as working electrodes. An Ag/AgCl/KCl (3 M) and a Pt mesh were used as reference and counter electrodes, respectively. At variance with our previous study on β-Fe_2O_3 nanostructures that were tested in Na_2SO_4 solutions, being unstable in alkaline media,[46] an aqueous NaOH solution (pH = 13.6), previously purged with N_2 for 30 min, was used as electrolyte. A PARSTAT 2273 potentiostat was used for current−voltage measurements under simulated solar light (AM 1.5G; irradiation intensity = 100 mW cm^{-2}).

Transmission electron microscopy (TEM) and electron diffraction (ED) experiments were carried out on a FEI Tecnai Osiris microscope, operated at 200 kV and equipped with a Super-X high solid angle energy dispersive X-ray (EDX) detector. High-angle annular dark field-scanning transmission electron microscopy (HAADF-STEM) and high resolution TEM (HRTEM) images were acquired on a FEI Titan "cubed" microscope (acceleration voltage = 300 kV), equipped with an aberration corrector for the probe-forming and image-forming lens.

TAS analyses were performed on specimens having a geometric area of 3 × 3 cm^2 in a complete PEC cell (Zahner-Elektrik PECC-2). To simulate the conditions of the above PEC experiments, a three-electrode configuration was used with a Pt counter electrode, an Ag/AgCl/KCl (3 M) reference electrode, and a NaOH electrolyte, degassed with N_2 prior to experiments. Measurements were carried out by a modified flash-photolysis apparatus (Luzchem LFP-111) with a New Focus (model 2051) photodetector and a halogen lamp (9 W, Thorlabs SLS201/M) probe (see also SI for further details).

RESULTS AND DISCUSSION

Initial efforts were devoted to the fabrication of α-Fe_2O_3 systems endowed with the following characteristics:[14] (a) improved crystallinity, with reduced content of charge trapping defects, (b) porous non-isotropic morphology, enabling a higher active area. The as-prepared materials appear semi-transparent and orange−red, and upon annealing at 650 °C a slight color darkening is observed.[5,29] Figure 1 displays XRD patterns of as-prepared and annealed systems. Apart from prominent peaks related to FTO that dominate the recorded patterns, the diffraction signals located at 2θ = 24.1, 33.1, 35.6, 40.8, and 49.4° can be attributed to (012), (104), (110), (113), and (024) reflections of the rhombohedral hematite phase, respectively.[56] No other signals could be observed, indicating the absence of other Fe_2O_3 polymorphs. Irrespective of the adopted growth temperature, thermal processing results in a progressive enhancement of the (110) reflection. This phenomenon, in accordance with previous observations,[10,43] may suggest a preferential alignment of the [110] axis perpendicularly to the substrate (being a *c*-oriented growth). In particular, the (110)/(012) intensity ratio, systematically higher than in the case of α-Fe_2O_3 powder diffractogram,[56] undergoes a progressive increase according to the order **300** < **400** < **300_A** < **400_A** (see Table 1). It has been reported that hematite has a much higher conductivity along the [110] direction with respect to the orthogonal ones such as [001] (Figure 1c).[25,36,45] As a consequence, the above-mentioned preferred orientation may account for an improved electron transport through annealed specimens, facilitating the collection of photogenerated electrons[4,5] and resulting in enhanced PEC performances (see below and Figure 6).[10,20]

To analyze the system chemical composition, XPS and SIMS analyses were carried out. Figure 2a compares representative XPS wide-scan spectra for the target materials before and after the annealing treatment. The analysis of the O/Fe ratio shows no statistically relevant evidence that oxygen deficiencies are

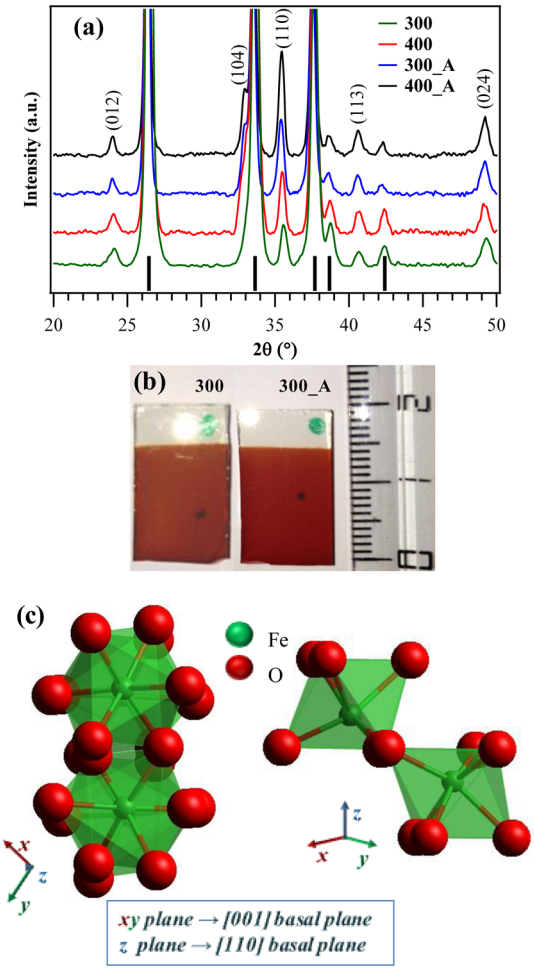

Figure 1. (a) XRD patterns of as-grown and annealed Fe_2O_3 specimens. Reflections pertaining to the FTO-coated glass substrate are marked by vertical bars. (b) Digital photographs of two obtained photoelectrode specimens before and after thermal treatment. (c) Representation of α-Fe_2O_3 structure,[56] characterized by octahedral arrangements of iron(III) centers.

playing a major role in the electrode photoactivity,[29] at variance with previous studies.[10] The average O/Fe values close to 1.7, slightly higher than the stoichiometric one expected for Fe_2O_3, were related to surface hydroxylation (see also Figure S1 in the SI). Irrespective of the experimental conditions, the Fe2p peak shape and position [BE($Fe2p_{3/2}$) = 711.2 eV], along with the spin orbit separation of 13.4 eV,[4,31,37,46,57] are in agreement with the presence of Fe(III) in an oxide environment, free from other iron oxidation states.[8,18,20,32,52,55,58] Preliminary studies on the in-depth system composition were carried out by XPS profiling on annealed systems. Regarding the O1s peak (Figure 2b), the high BE tailing disappears after erosion, confirming that it arises from atmospheric exposure. The depth profile of the Fe2p region (Figure 2c) shows no significant variation, in line with the presence of pure iron(III) oxide in the target material. The good sample purity is confirmed also by the strong decrease of the C1s peak intensity upon sputtering (Figure S2 in the SI).

More detailed information on the in-depth distribution of the various species was obtained by SIMS, and representative data are displayed in Figure 3. As a general rule, the specimen purity increases after thermal treatment, resulting in average carbon content as low as tenths of ppm. Irrespective of the sample

DOI: 10.1021/acsami.5b00919
ACS Appl. Mater. Interfaces 2015, 7, 8667−8676

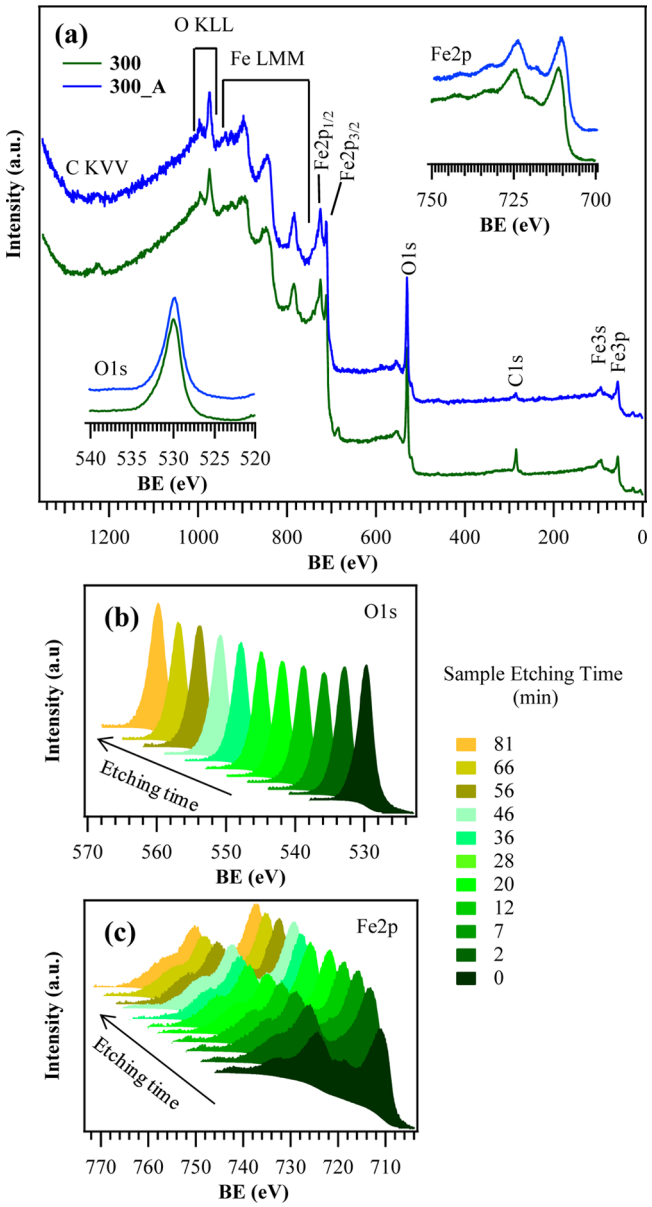

Figure 2. (a) Representative surface XPS survey spectra for as-prepared and annealed Fe_2O_3 specimens grown at 300 °C. Insets display the corresponding Fe2p and O1s spectral regions. (b,c) XPS depth profiles for the annealed α-Fe_2O_3 sample prepared at 300 °C, showing the O1s and Fe2p photopeak evolution as a function of the etching time.

processing conditions, profiling in different specimen regions reveals a parallel trend of Fe and O signals, suggesting their common chemical origin and confirming the homogeneous formation of iron(III) oxide, as also revealed by XPS. In addition, the data evidence a Sn tail extending into the nanodeposits, suggesting Sn diffusion from the FTO substrate into the material, at least to some extent. This phenomenon, improving, in turn, the system electrical conductivity[4,5,36] and speeding up the interfacial reaction of photogenerated holes,[16] might result beneficial in view of PEC applications.[31]

Efforts were subsequently dedicated to the analysis of the deposit morphology through the combined use of AFM and FE-SEM (Figure 4). For specimens grown at 300 °C, AFM measurements reveal a fine arrangement of homogeneous nanoaggregates. The micrograph elaboration enables to extract

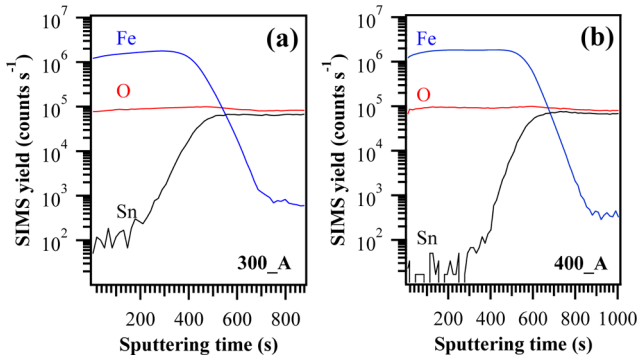

Figure 3. Fe, O, and Sn SIMS depth profiles for Fe_2O_3 specimens deposited at 300 °C (a) and 400 °C (b), after thermal treatment.

RMS roughness values, an important parameter in view of PEC applications[12] because an enhanced roughness is expected to correspond to a higher electrode/electrolyte interfacial area.[35] The values obtained in the present case are all very close to (20.0 ± 1.5) nm and do not display any marked dependence on the processing conditions. To attain a deeper insight into the material morphology, FE-SEM analyses were undertaken, devoting particular attention not only to plane-view but also to cross-sectional observations that are often missing in reports devoted to FTO-supported photoelectrodes.[5,10,19−21,29,35] The results (Figure 4) evidence a system of nano-organization based on two levels of hierarchical growth. In fact, sample **300** shows the presence of pyramidal aggregates as the smaller building blocks, possessing average dimensions of (80 ± 20) nm. These particles are interconnected forming larger agglomerates with a mean length of (400 ± 100) nm and giving rise to a tightly packed cross-sectional arrangement. Similarly, specimen **400** displays the presence of dendritic structures [average sizes = (85 ± 20) nm and (500 ± 100) nm for the primary and secondary particles, respectively] evenly distributed over the FTO substrate. As shown by cross-sectional images, such dendrites appear vertically aligned with respect to the substrate, producing a relatively porous morphology. Such nanostructures may facilitate carrier transport, allowing photogenerated holes to efficiently reach the interface with the electrolyte and improving the rate of charge transport relative to recombination.[7,43] The presence of similar vertical arrays has also been reported to be beneficial for light trapping and scattering phenomena,[21] which, in turn, enhance the nanomaterial light harvesting properties (see below).

In line with previous reports,[10] the images of annealed samples demonstrate that the primary particles are bigger, more rounded, and partially merged together, an effect more evident for specimen **300_A**. In this case, the morphology is dominated by the presence of rounded elongated aggregates of (170 ± 60) nm. For 400 °C-deposited systems, a relatively similar particle structure is observed, although their morphology and shape are more reminiscent of the pristine nanodeposits, as evidenced by the bumped edges of larger agglomerates.

Despite RMS roughness values are very similar for all specimens (see above), cross-sectional FE-SEM micrographs registered after thermal treatment display the formation of more porous systems. The **300_A** sample shows structures more rounded than in the pristine specimen, with the base areas almost fused into larger agglomerates. For the **400_A** sample, this effect is slightly less pronounced, resulting in the formation of multiparticle agglomerates [primary particle

DOI: 10.1021/acsami.5b00919
ACS Appl. Mater. Interfaces 2015, 7, 8667−8676

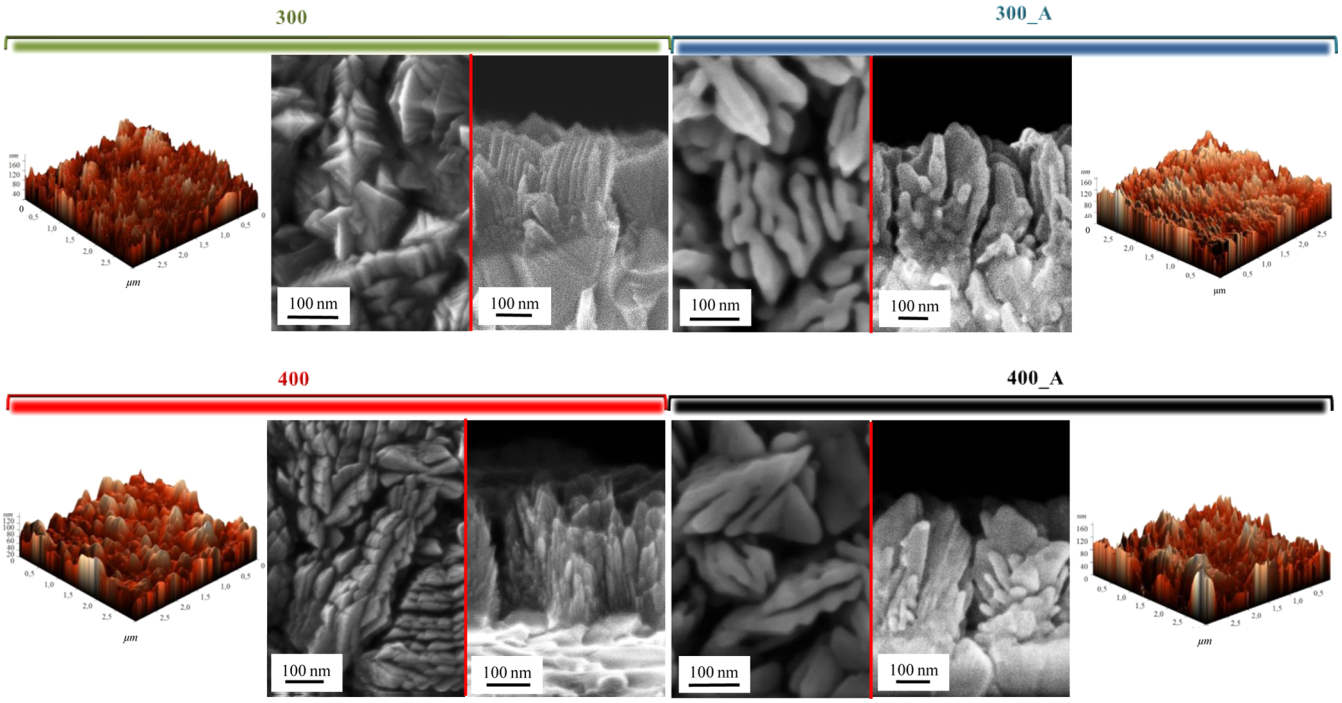

Figure 4. AFM and FE-SEM images for α-Fe_2O_3 nanodeposits grown at 300 and 400 °C, before and after thermal treatment.

average sizes = (90 ± 30) nm; larger agglomerate dimensions = (450 ± 100) nm]. Correspondingly, an increase in the mean nanodeposit thickness is observed (see Table 1). Overall, the annealing process seems to result in significant rearrangements leading to a decrease in grain boundary density, a phenomenon favorable for the system PEC performances (see below and Figure 6)[14] because it suppresses the recombination of photogenerated charge carriers.[7,20]

Because the optical absorption features of α-Fe_2O_3 are of great importance for solar energy conversion,[29] the target nanosystems were also analyzed by optical absorption spectroscopy (Figure 5). The absorption profiles are characterized by a sub-band gap scattering tail in the 600−750 nm region,[29] which becomes more intense upon annealing for both nanodeposits fabricated at 300 and 400 °C. Concomitantly, data reveal the enhancement of a shoulder centered at $\lambda \approx 540$ nm, typical of α-Fe_2O_3 films,[7] related to spin-forbidden Fe(III) 3d → 3d transitions.[10,14,19,43] For all specimens, a sharp absorbance increase occurs from 550−600 nm toward lower wavelengths, consistently with the band gap of hematite (see also below).[12,14,58] In addition, in accordance with previous findings,[29,43] the absorption coefficient (α, see SI, section S-2.2) undergoes a systematic enhancement with the adopted processing temperature, i.e., according to the order **300** < **400** < **300_A** < **400_A** (see Table 1). This phenomenon is of great importance, taking into account that a superior Vis light absorption efficiency is one of the key factors positively influencing PEC performances.[5,29,30,43] In particular, such a trend can be related to an increase of light scattering for the formation of hierarchical structures, as previously discussed.[21] The increase of light absorption, however, cannot be traced back to the sole increase in particle size observed by FE-SEM analyses[29] and is also determined by an increase in the system crystallinity with processing temperature (compare XRD and TEM results, Figures 1 and 7).

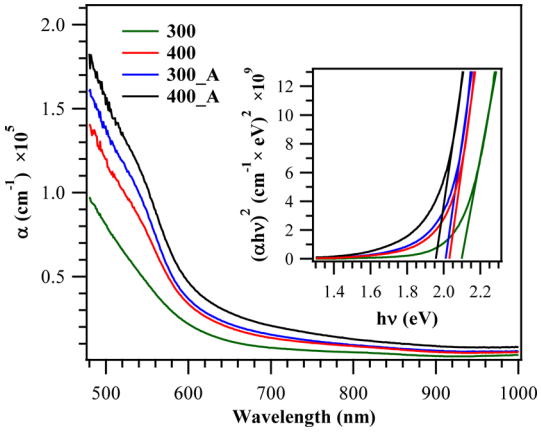

Figure 5. Optical absorption spectra for as-prepared and annealed Fe_2O_3 nanodeposits. Inset: Tauc plot of $(\alpha h\nu)^2$ vs $h\nu$ for the same specimens. The lines fitted to the linear portion of these plots shows the optical band gap approximation.

The effects of the processing temperature on light absorption properties are further evidenced by Tauc plots reported in the inset of Figure 6 (see also SI), enabling extrapolation of optical band gaps. The E_G values, in good agreement with previous reports on hematite,[4,9,19,20,31,36,37] decrease according to the order **300** > **400** > **300_A** > **400_A** (Table 1). In addition, a slight increase in the slope of the transition upon annealing (see Figure 5) is also observed. In the Tauc relation (equation S1 in the SI), the slope is proportional to the band tailing parameter, which, in turn, is related to the distribution of energy states near the valence and conduction band edges.[29] Its increase, as well as the above band gap variations, are both due to an increased material crystallinity and particle size occurring after thermal treatment.[10,59,60]

Further important clues are provided by an analysis of the optical penetration depth (α^{-1}) values (defined as the distance over which 63% of the photons of wavelength λ are

DOI: 10.1021/acsami.5b00919
ACS Appl. Mater. Interfaces 2015, 7, 8667−8676

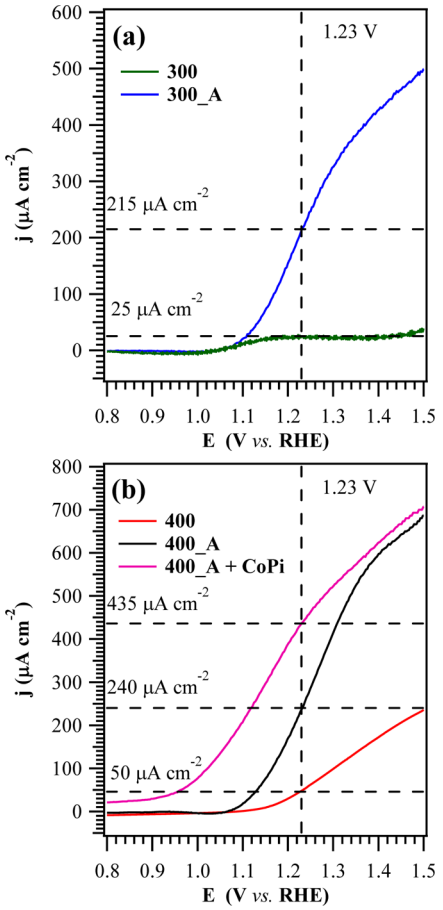

Figure 6. Photocurrent density vs applied potential curves for: (a) Fe_2O_3 nanodeposits grown at 300 °C, before and after thermal treatment; (b) as-prepared and annealed Fe_2O_3 specimens deposited at 400 °C, eventually functionalized with Co-Pi cocatalyst. For sake of clarity, the j values at 1.23 V vs the reversible hydrogen electrode (RHE), i.e., at the theoretical water oxidation potential, are marked in each case by dashed lines.

absorbed;[34,52] equation S2 in the SI). The values obtained at λ = 500 nm (Table 1) agree reasonably well with previous data for α-Fe_2O_3 systems.[10,46] In the present study, α^{-1} values monotonically decrease according to the order **300** > **400** > **300_A** > **400_A**, likely resulting in an enhanced system photoefficiency.[7,46]

PEC performances of the target materials were evaluated by measuring the current−voltage characteristics in the dark and under irradiation. In general, dark currents (not reported) are 2 orders of magnitude lower than the ones under illumination. Photocurrent density vs applied voltage curves for front side illumination are displayed in Figure 6. Irrespective of the deposition temperature, a systematic photoresponse increase is observed upon thermal treatment, indicating a beneficial influence of the latter on functional performances. For 300 °C-grown materials (Figure 6a), photocurrent values undergo an appreciable enhancement after annealing (compare Table 1). For samples fabricated at 400 °C, the resulting photocurrent increase upon thermal treatment was lower (nearly 5-fold), but higher j values were obtained after annealing (compare j values of **300_A** vs **300** and of **400_A** vs **400** in Table 1). In this case, the photocurrent onset shifts by about 0.1 V to negative potential after annealing, thus improving the j values at lower bias voltages, as recently reported for hematite-based nanosheet arrays.[43]

Despite some investigators obtained higher photocurrent values for Fe_2O_3-based materials,[4,12,14,20,21] the photoefficiency of the **400_A** specimen (j ≈ 680 μA cm^{-2} at 1.50 V) is higher not only than various bare Fe_2O_3 photoelectrodes treated at similar temperatures[1,5,9,10,17,23,29,37,43,46] but also than some hematite films either doped[16,18,19,31] or functionalized[13,24,35] with various agents. Remarkably, the present materials compare very favorably also with Fe_2O_3 photoanodes prepared by AP-CVD that yield similar or lower photocurrent values.[2,34,48−51] These findings highlight the potential of the proposed fabrication route for the production of α-Fe_2O_3 photoanodes with reasonable efficiency even without any dopants under milder annealing conditions (T < 700 °C) than those often reported.

Subsequently, in a preliminary attempt to further optimize the present hematite systems,[12] the most active sample, i.e., **400_A**, was additionally functionalized with Co-Pi (SI, section S-1), a well-known oxygen evolution catalyst.[22,35,36] As shown in Figure 6b, upon functionalization with Co-Pi, the photocurrent density at 1.23 V vs RHE undergoes an 80% enhancement, and the potential shows a cathodic shift of ≈0.2 V. In line with previous reports on hematite functionalized by Co-Pi,[17,30,36] Ir oxide,[12] or $NiFeO_x$,[27] these variations reflect the activity of Co-Pi as a catalyst for the oxygen evolution reaction, speeding up the reaction kinetics and reducing carrier recombination.[17,35]

To investigate the time stability of the present materials, PEC measurements were repeated under the same experimental conditions at the first and third day for the best performing systems, i.e., specimens **400_A** and **400_A + CoPi**. The results (Figure S4 in the SI) evidence that the measured photocurrent values are almost unchanged as a function of time, revealing a good stability of the target photoanodes, an important prerequisite for their practical applications.

Overall, PEC data discussed so far indicate that the system photoresponse increases according to the following order: **300** < **400** < **300_A** < **400_A** (see Table 1). The photoefficiency improvement with increasing processing temperature can be ascribed to a concurrence of different effects:[5,14,21,29,31,36]

i. the increase in crystallinity and in the (110) preferential orientation, following the same order (compare XRD/TEM results and Table 1);
ii. the morphological rearrangement evidenced by FE-SEM data (see Figure 4 and the related discussion), with particular regard to the porosity increase and the concomitant reduction of grain boundary density;
iii. the systematic enhancement of the absorption coefficient with annealing temperature and the parallel decrease of the optical band gap (Figure 5 and Table 1).

The information gathered so far can explain the obtained order of PEC performances for the samples. Nevertheless, other factors, such as electron transport limitations and recombination centers, can play a crucial role in determining the functional behavior of hematite.[7] In this regard, a further investigation of the system nanoscale evolution upon annealing and of its impact on the photogenerated charge carrier kinetics is of major importance. To gain a deeper insight into these issues, TEM and TAS analyses were carried out on two selected samples, namely **300** and **300_A**. These specimens were chosen taking into account that they present a higher

DOI: 10.1021/acsami.5b00919
ACS Appl. Mater. Interfaces 2015, 7, 8667−8676

photoresponse increase upon annealing with respect to nanodeposits fabricated at 400 °C (see Figure 6 and Table 1). The nanoscale morphology and composition of the selected α-Fe_2O_3 deposits was investigated by TEM. Parts a and b of Figure 7 display HAADF-STEM images, also referred to as *Z*-contrast or mass-thickness contrast images, of as-prepared and annealed materials. The samples clearly consist of three layers, a glass substrate, the FTO layer, and the top Fe_2O_3 nanodeposit, whose chemical nature is confirmed by the pertaining EDX map (Figure 7a, inset, and Figure S5 in the SI). In agreement with XRD data (see above), ED characterization (Figure 7c, inset) confirms that the only crystalline phase is α-Fe_2O_3.[56] The ED rings of the as-prepared sample demonstrate the polycrystalline nature of the Fe_2O_3 system.

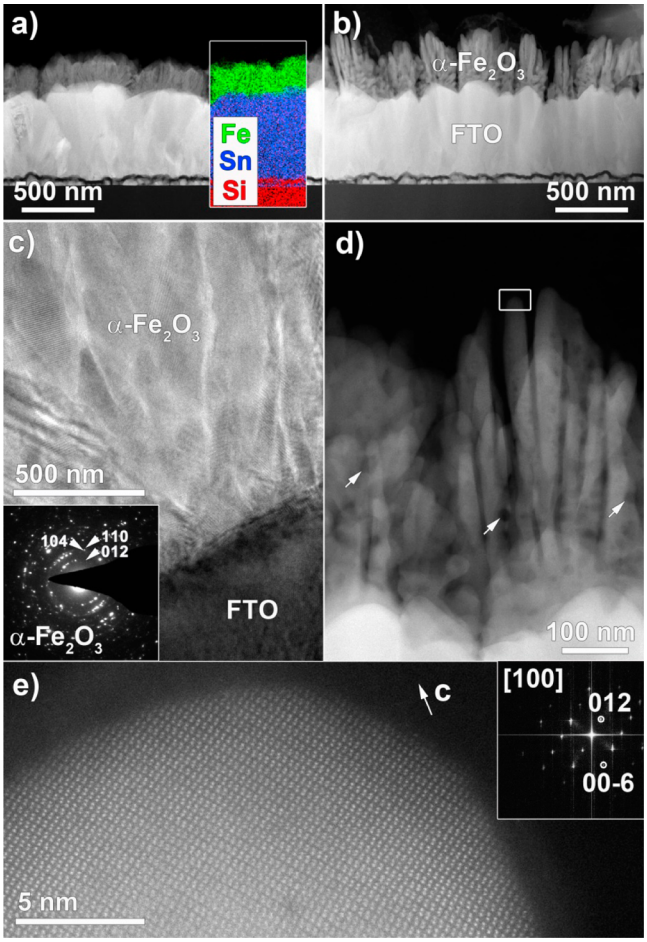

Figure 7. TEM characterization of as-prepared and annealed α-Fe_2O_3 nanodeposits fabricated at 300 °C. (a) Cross-sectional HAADF-STEM image of sample **300**, with EDX chemical map displayed in the inset. (b) Cross-sectional HAADF-STEM micrograph of specimen **300_A**. (c) Bright-field TEM image of the FTO/α-Fe_2O_3 interface for sample **300**. Inset: ED pattern of the α-Fe_2O_3 nanodeposit. (d) Representative HAADF-STEM image of α-Fe_2O_3 dendrites in specimen **300_A**. White arrows mark the presence of some low-contrast pores. (e) High resolution HAADF-STEM micrograph of a α-Fe_2O_3 dendrite in sample **300_A**. The image is taken from the region marked by the white rectangle in (d).

A detailed inspection reveals that thermal treatment induces a significant increase of the nanodeposits porosity, a very beneficial effect in terms of PEC performances (compare Figure 6 and the above discussion). Before thermal treatment (Figure 7a,c), the α-Fe_2O_3 nanodeposit was thinner and relatively dense (see also Table 1). In a different way, the homologous annealed system (Figure 7b,d) appears less dense and forms dendritic structures (see also FE-SEM data). The presence of low-contrast pores inside the target nanostructures can also be clearly observed (see Figure 7d). Additionally, the crystallinity undergoes a parallel enhancement upon annealing, as illustrated by the high resolution HAADF-STEM image of a typical α-Fe_2O_3 dendrite (Figure 7e), in agreement with XRD data. The inset Fourier Transform pattern confirms that the dendrite is imaged along the [100] α-Fe_2O_3 zone axis orientation. The preferred exposure of {110}-type surface facets, as suggested by XRD results, is a result of the near *c*-oriented growth of most of the dendrites (see also Figure S6 in the SI).

To analyze the kinetics of photoproduced charge carriers and elucidate the interrelations with the system PEC behavior, TAS analyses were carried out on specimens deposited at 300 °C, before and after annealing. Figure 8 shows the transient absorption decays of the hematite photoelectrodes, following the band gap excitation laser pulse. On a ms time scale (Figure 8a), a strong absorption bleaching (negative absorption change) is observed and attributed to a decreased ground state absorption caused, in turn, by trapped photoelectrons a few hundred mV below the conduction band edge.[26,41,42] Exponential fits of the bleaching recovery (Figure 8c) yield lifetimes of (1.7 ± 0.4) ms and (1.9 ± 0.7) ms for as-prepared and annealed specimens, respectively, suggesting similar recombination dynamics on a ms time scale. The main difference between these TAS signals is the strong transient absorption observed for the annealed sample 5 ms after excitation, which is even more pronounced on a second time scale (Figure 8b). The positive absorption change corresponds to photoholes surviving bulk recombination, possessing a sufficient lifetime to participate to the PEC H_2O splitting (Figure 8d).[15] Using a simple monoexponential fit, a lifetime of (3 ± 1) s is determined for photogenerated holes contributing to water oxidation. As observed in Figure 8b, the number of long-lived holes appreciably increases after annealing, providing a key explanation about the impact of annealing on the charge carrier lifetime.

Figure 8c presents absorption decay component spectra of hematite photoelectrodes derived by global mono- (**300**) and biexponential fits (**300_A**) of transient decays on a ms time scale and the calculated transient spectrum at 0 ms delay. The biexponential model was adopted to fit also the decay of positive transient hole absorption of the annealed sample (Figure 8b). The transient spectra at 0 ms and τ_1 = 1.7 ms of trapped electrons at λ = 580 nm and photoholes at λ > 650 nm are similar for both samples, suggesting an equal number of charges in the sub-ms time scale, indicating that thermal treatments do not alter primary electron−hole recombination processes on a time range faster than μs.

The transient component spectrum of τ_1 = 1.9 ms is mainly attributed to recombination of the photoelectrons, resulting in the final transient state of τ_2 = 3 s (**300_A**) in Figure 8c. The broad and shapeless transient absorption of the final state corresponds to the absorption of long-lived holes with no remaining trapped electron absorption at λ = 580 nm. The absorption amplitude indicates that roughly half of the holes in a ms time scale (spectrum at 0 ms) survive to the recombination processes and have a lifetime in the second time range. The bleaching recovery, i.e., the disappearance of photogenerated trapped electron absorption, is due to electron

DOI: 10.1021/acsami.5b00919
ACS Appl. Mater. Interfaces 2015, 7, 8667−8676

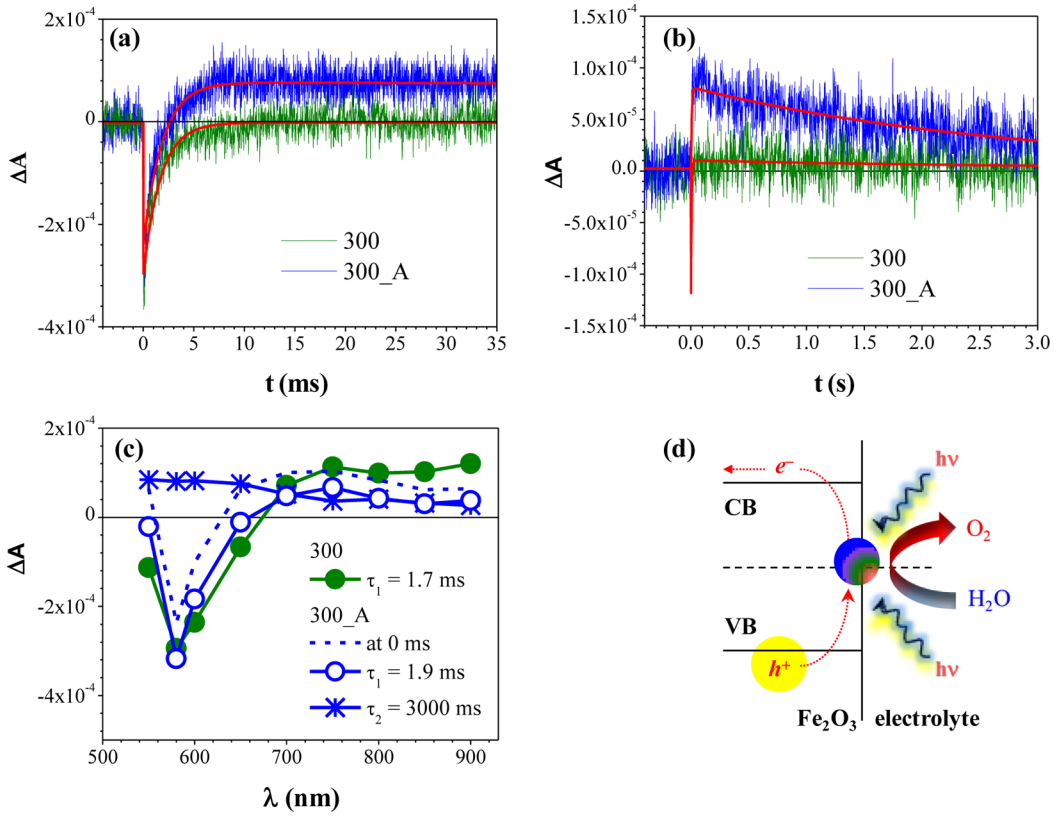

Figure 8. (a) Transient absorption decays at λ = 580 nm on a ms time scale for as-prepared and annealed Fe_2O_3 nanodeposits grown at 300 °C. (b) The corresponding decays in a second time scale. Exponential fits are also displayed. (c) Absorption decay component of spectra at 1.6 V vs RHE for as-prepared and annealed Fe_2O_3 nanodeposits grown at 300 °C. The transient absorption spectrum at zero delay time, following the laser pulse excitation, is shown for the **300_A** sample as the calculated spectrum at 0 ms. (d) Simplified illustration of the photogenerated processes taking place at a photoelectrode−electrolyte interface in PEC water splitting.

extraction into the external electrical circuit,[26,42] resulting in photoholes with a prolonged lifetime of 3 s. The obtained lifetime is in line with previously reported values for similar systems.[2] On the basis of these data, thermal treatment is suggested to increase the electron mobility in the target hematite systems, thus hindering electron−hole recombination (i.e., producing an enhanced electron extraction). The resulting long-lived holes contributing to the transient absorption have a sufficient lifetime to participate to the PEC H_2O oxidation (Figure 8d), as reflected by the significant photoresponse enhancement after annealing (Figure 6). Conversely, the as-prepared **300** photoelectrode has a negligible PEC activity, as there is no evidence of long-lived photoholes in this case.

CONCLUSIONS

Single-phase hematite nanostructures were fabricated on FTO substrates via single-step PE-CVD at temperatures of 300 and 400 °C, followed by thermal treatment in air at 650 °C. The proposed approach yielded nanosystems with hierarchical morphologies that could be finely tailored as a function of the annealing process, resulting in an enhancement of the (110) orientation and of the overall porosity. The best performing systems in PEC H_2O splitting were the most crystalline materials, characterized by the highest porosity and light harvesting capabilities. Importantly, TAS analyses, performed for the first time on PE-CVD Fe_2O_3 nanostructures, revealed that the annealing process favorably affected photogenerated charge carriers dynamics, resulting in long-lived holes (lifetimes >1 s) positively contributing to H_2O oxidation. The system functional performances, characterized also by a good time stability, could be further improved by functionalization with a Co-Pi overlayer, amplifying the measured photocurrent and reducing the onset potential.

Our results demonstrate the possibility of tailoring the PEC water splitting activity of α-Fe_2O_3 photoelectrodes, providing useful clues on the important parameters to be tuned in order to develop more efficient PEC devices. In particular, the activities of the present systems are prone to further increase by optimization of the synthetic procedure, with particular focus on lower feature sizes closer to the hole diffusion length. In addition, further efforts will be devoted to the introduction of metal dopants and the functionalization with suitable layers, leading to a higher performance boost in the sustainable storage of solar energy through water splitting processes.

ASSOCIATED CONTENT

Supporting Information

Details on synthesis, XPS, optical absorption, PEC, EDX, TEM, and TAS characterization. This material is available free of charge via the Internet at http://pubs.acs.org.

AUTHOR INFORMATION

Corresponding Author

*Phone: 39-049-8275170. Fax: 39-049-8275161. E-mail: davide.barreca@unipd.it.

Notes

The authors declare no competing financial interest.

DOI: 10.1021/acsami.5b00919
ACS Appl. Mater. Interfaces 2015, 7, 8667−8676

■ ACKNOWLEDGMENTS

We acknowledge financial support under the Seventh Framework Program (FP7) by the project "SOLAROGENIX" (NMP4-SL-2012-310333) and the ERC grant no. 246791, COUNTATOMS. This work was further funded by Padova University ex-60% 2012−2014 and SOLLEONE (CPDR132937/13) projects, as well as by Regione Lombardia-INSTM ATLANTE program and the Fund for Scientific Research Flanders (FWO). Many thanks are also due to Prof. J. R. Morante, Dr. D. Monllor-Satoca, Dr. C. Fàbrega, and Dr. T. Andreu (IREC, Sant Adrià de Besòs, Spain) for the precious help and assistance in PEC measurements.

■ REFERENCES

(1) Riha, S. C.; Klahr, B. M.; Tyo, E. C.; Seifert, S.; Vajda, S.; Pellin, M. J.; Hamann, T. W.; Martinson, A. B. F. Atomic Layer Deposition of a Submonolayer Catalyst for the Enhanced Photoelectrochemical Performance of Water Oxidation with Hematite. *ACS Nano* **2013**, *7*, 2396−2405.

(2) Cowan, A. J.; Barnett, C. J.; Pendlebury, S. R.; Barroso, M.; Sivula, K.; Grätzel, M.; Durrant, J. R.; Klug, D. R. Activation Energies for the Rate-Limiting Step in Water Photooxidation by Nanostructured α-Fe_2O_3 and TiO_2. *J. Am. Chem. Soc.* **2011**, *133*, 10134−10140.

(3) Lee, J.; Mubeen, S.; Ji, X.; Stucky, G. D.; Moskovits, M. Plasmonic Photoanodes for Solar Water Splitting with Visible Light. *Nano Lett.* **2012**, *12*, 5014−5019.

(4) Mirbagheri, N.; Wang, D.; Peng, C.; Wang, J.; Huang, Q.; Fan, C.; Ferapontova, E. E. Visible Light Driven Photoelectrochemical Water Oxidation by Zn- and Ti-Doped Hematite Nanostructures. *ACS Catal.* **2014**, *4*, 2006−2015.

(5) Ling, Y.; Wang, G.; Wheeler, D. A.; Zhang, J. Z.; Li, Y. Sn-Doped Hematite Nanostructures for Photoelectrochemical Water Splitting. *Nano Lett.* **2011**, *11*, 2119−2125.

(6) Wheeler, D. A.; Wang, G.; Ling, Y.; Li, Y.; Zhang, J. Z. Nanostructured Hematite: Synthesis, Characterization, Charge Carrier Dynamics, and Photoelectrochemical Properties. *Energy Environ. Sci.* **2012**, *5*, 6682−6702.

(7) Hahn, N. T.; Ye, H.; Flaherty, D. W.; Bard, A. J.; Mullins, C. B. Reactive Ballistic Deposition of α-Fe_2O_3 Thin Films for Photoelectrochemical Water Oxidation. *ACS Nano* **2010**, *4*, 1977−1986.

(8) Mettenbörger, A.; Singh, T.; Singh, A. P.; Järvi, T. T.; Moseler, M.; Valldor, M.; Mathur, S. Plasma-Chemical Reduction of Iron Oxide Photoanodes for Efficient Solar Hydrogen Production. *Int. J. Hydrogen Energy* **2014**, *39*, 4828−4835.

(9) Singh, A. P.; Mettenbörger, A.; Golus, P.; Mathur, S. Photoelectrochemical Properties of Hematite Films Grown by Plasma Enhanced Chemical Vapor Deposition. *Int. J. Hydrogen Energy* **2012**, *37*, 13983−13988.

(10) Rajendran, R.; Yaakob, Z.; Pudukudy, M.; Rahaman, M. S. A.; Sopian, K. Photoelectrochemical Water Splitting Performance of Vertically Aligned Hematite Nanoflakes Deposited on FTO by a Hydrothermal Method. *J. Alloys Compd.* **2014**, *608*, 207−212.

(11) Emery, J. D.; Schlepütz, C. M.; Guo, P.; Riha, S. C.; Chang, R. P. H.; Martinson, A. B. F. Atomic Layer Deposition of Metastable β-Fe_2O_3 via Isomorphic Epitaxy for Photoassisted Water Oxidation. *ACS Appl. Mater. Interface* **2014**, *6*, 21894−21900.

(12) Marelli, M.; Naldoni, A.; Minguzzi, A.; Allieta, M.; Virgili, T.; Scavia, G.; Recchia, S.; Psaro, R.; Dal Santo, V. Hierarchical Hematite Nanoplatelets for Photoelectrochemical Water Splitting. *ACS Appl. Mater. Interfaces* **2014**, *6*, 11997−12004.

(13) Steier, L.; Herraiz-Cardona, I.; Gimenez, S.; Fabregat-Santiago, F.; Bisquert, J.; Tilley, S. D.; Grätzel, M. Understanding the Role of Underlayers and Overlayers in Thin Film Hematite Photoanodes. *Adv. Funct. Mater.* **2014**, *24*, 7681−7688.

(14) Kim, J. Y.; Magesh, G.; Youn, D. H.; Jang, J.-W.; Kubota, J.; Domen, K.; Lee, J. S. Single-crystalline, Wormlike Hematite Photoanodes for Efficient Solar Water Splitting. *Sci. Rep.* **2013**, *3*, 2681.

(15) Cowan, A. J.; Durrant, J. R. Long-lived Charge Separated States in Nanostructured Semiconductor Photoelectrodes for the Production of Solar Fuels. *Chem. Soc. Rev.* **2013**, *42*, 2281−2293.

(16) Dunn, H. K.; Feckl, J. M.; Muller, A.; Fattakhova-Rohlfing, D.; Morehead, S. G.; Roos, J.; Peter, L. M. P.; Scheu, C.; Bein, T. Tin Doping Speeds up Hole Transfer During Light-Driven Water Oxidation at Hematite Photoanodes. *Phys. Chem. Chem. Phys.* **2014**, *16*, 24610−24620.

(17) Hamann, T. W. Splitting Water with Rust: Hematite Photoelectrochemistry. *Dalton Trans.* **2012**, *41*, 7830−7834.

(18) Liu, J.; Liang, C.; Xu, G.; Tian, Z.; Shao, G.; Zhang, L. Ge-doped Hematite Nanosheets with Tunable Doping Level, Structure and Improved Photoelectrochemical Performance. *Nano Energy* **2013**, *2*, 328−336.

(19) Shen, S.; Kronawitter, C.; Jiang, J.; Mao, S.; Guo, L. Surface Tuning for Promoted Charge Transfer in Hematite Nanorod Arrays as Water-Splitting Photoanodes. *Nano Res.* **2012**, *5*, 327−336.

(20) Hsu, Y.-P.; Lee, S.-W.; Chang, J.-K.; Tseng, C.-J.; Lee, K.-R.; Wang, C.-H. Effects of Platinum Doping on the Photoelectrochemical Properties of Fe_2O_3 Electrodes. *Int. J. Electrochem. Sci.* **2013**, *8*, 11615−11623.

(21) Park, S.; Kim, H. J.; Lee, C. W.; Song, H. J.; Shin, S. S.; Seo, S. W.; Park, H. K.; Lee, S.; Kim, D.-W.; Hong, K. S. Sn Self-Doped α-Fe_2O_3 Nanobranch Arrays Supported on a Transparent, Conductive SnO_2 Trunk to Improve Photoelectrochemical Water Oxidation. *Int. J. Hydrogen Energy* **2014**, *39*, 16459−16467.

(22) Sivula, K.; Le Formal, F.; Grätzel, M. Solar Water Splitting: Progress Using Hematite (α-Fe_2O_3) Photoelectrodes. *ChemSusChem* **2011**, *4*, 432−449.

(23) Liu, J.; Shahid, M.; Ko, Y.-S.; Kim, E.; Ahn, T. K.; Park, J. H.; Kwon, Y.-U. Investigation of Porosity and Heterojunction Effects of a Mesoporous Hematite Electrode on Photoelectrochemical Water Splitting. *Phys. Chem. Chem. Phys.* **2013**, *15*, 9775−9782.

(24) Tallarida, M.; Das, C.; Cibrev, D.; Kukli, K.; Tamm, A.; Ritala, M.; Lana-Villarreal, T.; Gómez, R.; Leskelä, M.; Schmeisser, D. Modification of Hematite Electronic Properties with Trimethyl Aluminum to Enhance the Efficiency of Photoelectrodes. *J. Phys. Chem. Lett.* **2014**, *5*, 3582−3587.

(25) LaTempa, T. J.; Feng, X.; Paulose, M.; Grimes, C. A. Temperature-Dependent Growth of Self-Assembled Hematite (α-Fe_2O_3) Nanotube Arrays: Rapid Electrochemical Synthesis and Photoelectrochemical Properties. *J. Phys. Chem. C* **2009**, *113*, 16293−16298.

(26) Le Formal, F.; Pendlebury, S. R.; Cornuz, M.; Tilley, S. D.; Grätzel, M.; Durrant, J. R. Back Electron−Hole Recombination in Hematite Photoanodes for Water Splitting. *J. Am. Chem. Soc.* **2014**, *136*, 2564−2574.

(27) Du, C.; Yang, X.; Mayer, M. T.; Hoyt, H.; Xie, J.; McMahon, G.; Bischoping, G.; Wang, D. Hematite-Based Water Splitting with Low Turn-On Voltages. *Angew. Chem. Int. Ed.* **2013**, *52*, 12692−12695.

(28) Nasibulin, A.; Rackauskas, S.; Jiang, H.; Tian, Y.; Mudimela, P.; Shandakov, S.; Nasibulina, L.; Jani, S.; Kauppinen, E. Simple and Rapid Synthesis of α-Fe_2O_3 Nanowires under Ambient Conditions. *Nano Res.* **2009**, *2*, 373−379.

(29) Sivula, K.; Zboril, R.; Le Formal, F.; Robert, R.; Weidenkaff, A.; Tucek, J.; Frydrych, J.; Grätzel, M. Photoelectrochemical Water Splitting with Mesoporous Hematite Prepared by a Solution-Based Colloidal Approach. *J. Am. Chem. Soc.* **2010**, *132*, 7436−7444.

(30) Qiu, Y.; Leung, S.-F.; Zhang, Q.; Hua, B.; Lin, Q.; Wei, Z.; Tsui, K.-H.; Zhang, Y.; Yang, S.; Fan, Z. Efficient Photoelectrochemical Water Splitting with Ultrathin Films of Hematite on Three-dimensional Nanophotonic Structures. *Nano Lett.* **2014**, *14*, 2123−2129.

(31) Shen, S.; Jiang, J.; Guo, P.; Kronawitter, C. X.; Mao, S. S.; Guo, L. Effect of Cr Doping on the Photoelectrochemical Performance of Hematite Nanorod Photoanodes. *Nano Energy* **2012**, *1*, 732−741.

DOI: 10.1021/acsami.5b00919
ACS Appl. Mater. Interfaces 2015, 7, 8667−8676

(32) Gao, G.; Zhang, Q.; Wang, K.; Song, H.; Qiu, P.; Cui, D. Axial Compressive α-Fe_2O_3 Microdisks Prepared from CSS Template for Potential Anode Materials of Lithium Ion Batteries. *Nano Energy* **2013**, *2*, 1010−1018.
(33) Low, Q. X.; Ho, G. W. Facile Structural Tuning and Compositing of Iron Oxide−Graphene Anode Towards Enhanced Supacapacitive Performance. *Nano Energy* **2014**, *5*, 28−35.
(34) Cesar, I.; Sivula, K.; Kay, A.; Zboril, R.; Grätzel, M. Influence of Feature Size, Film Thickness, and Silicon Doping on the Performance of Nanostructured Hematite Photoanodes for Solar Water Splitting. *J. Phys. Chem. C* **2009**, *113*, 772−782.
(35) Fu, L.; Yu, H.; Zhang, C.; Shao, Z.; Yi, B. Cobalt Phosphate Group Modified Hematite Nanorod Array as Photoanode for Efficient Solar Water Splitting. *Electrochim. Acta* **2014**, *136*, 363−369.
(36) Wang, L.; Lee, C.-Y.; Schmuki, P. Influence of Annealing Temperature on Photoelectrochemical Water Splitting of α-Fe_2O_3 Films Prepared by Anodic Deposition. *Electrochim. Acta* **2013**, *91*, 307−313.
(37) Fu, Z.; Jiang, T.; Liu, Z.; Wang, D.; Wang, L.; Xie, T. Highly Photoactive Ti-Doped α-Fe_2O_3 Nanorod Arrays Photoanode Prepared by a Hydrothermal Method for Photoelectrochemical Water Splitting. *Electrochim. Acta* **2014**, *129*, 358−363.
(38) Pendlebury, S. R.; Cowan, A. J.; Barroso, M.; Sivula, K.; Ye, J.; Grätzel, M.; Klug, D. R.; Tang, J.; Durrant, J. R. Correlating Long-Lived Photogenerated Hole Populations with Photocurrent Densities in Hematite Water Oxidation Photoanodes. *Energy Environ. Sci.* **2012**, *5*, 6304−6312.
(39) Joly, A. G.; Williams, J. R.; Chambers, S. A.; Xiong, G.; Hess, W. P.; Laman, D. M. Carrier Dynamics in α-Fe_2O_3 (0001) Thin Films and Single Crystals Probed by Femtosecond Transient Absorption and Reflectivity. *J. Appl. Phys.* **2006**, *99*, 053521.
(40) He, Y. P.; Miao, Y. M.; Li, C. R.; Wang, S. Q.; Cao, L.; Xie, S. S.; Yang, G. Z.; Zou, B. S.; Burda, C. Size and Structure Effect on Optical Transitions of Iron Oxide Nanocrystals. *Phys. Rev. B* **2005**, *71*, 125411.
(41) Pendlebury, S. R.; Wang, X.; Le Formal, F.; Cornuz, M.; Kafizas, A.; Tilley, S. D.; Grätzel, M.; Durrant, J. R. Ultrafast Charge Carrier Recombination and Trapping in Hematite Photoanodes under Applied Bias. *J. Am. Chem. Soc.* **2014**, *136*, 9854−9857.
(42) Barroso, M.; Pendlebury, S. R.; Cowan, A. J.; Durrant, J. R. Charge Carrier Trapping, Recombination and Transfer in Hematite (α-Fe_2O_3) Water Splitting Photoanodes. *Chem. Sci.* **2013**, *4*, 2724−2734.
(43) Liu, J.; Cai, Y. Y.; Tian, Z. F.; Ruan, G. S.; Ye, Y. X.; Liang, C. H.; Shao, G. S. Highly Oriented Ge-Doped Hematite Nanosheet Arrays for Photoelectrochemical Water Oxidation. *Nano Energy* **2014**, *9*, 282−290.
(44) Luan, P.; Xie, M.; Fu, X.; Qu, Y.; Sun, X.; Jing, L. Improved Photoactivity of TiO_2−Fe_2O_3 Nanocomposites for Visible-Light Water Splitting after Phosphate Bridging and its Mechanism. *Phys. Chem. Chem. Phys.* **2015**, *17*, 5043−5050.
(45) Cornuz, M.; Grätzel, M.; Sivula, K. Preferential Orientation in Hematite Films for Solar Hydrogen Production via Water Splitting. *Chem. Vap. Deposition* **2010**, *16*, 291−295.
(46) Barreca, D.; Carraro, G.; Gasparotto, A.; Maccato, C.; Sada, C.; Singh, A. P.; Mathur, S.; Mettenbörger, A.; Bontempi, E.; Depero, L. E. Columnar Fe_2O_3 Arrays via Plasma-Enhanced Growth: Interplay of Fluorine Substitution and Photoelectrochemical Properties. *Int. J. Hydrogen Energy* **2013**, *38*, 14189−14199.
(47) Park, S.; Kim, D.; Lee, C.; Seo, S.-D.; Kim, H.; Han, H.; Hong, K.; Kim, D.-W. Surface-Area-Tuned, Quantum-Dot-Sensitized Heterostructured Nanoarchitectures for Highly Efficient Photoelectrodes. *Nano Res.* **2014**, *7*, 144−153.
(48) Tahir, A. A.; Mat-Teridi, M. A.; Wijayantha, K. G. U. Photoelectrochemical Properties of Texture-Controlled Nanostructured α-Fe_2O_3 Thin Films Prepared by AACVD. *Phys. Status Solidi R* **2014**, *8*, 976−981.
(49) Saremi-Yarahmadi, S.; Wijayantha, K. G. U.; Tahir, A. A.; Vaidhyanathan, B. Nanostructured α-Fe_2O_3 Electrodes for Solar Driven Water Splitting: Effect of Doping Agents on Preparation and Performance. *J. Phys. Chem. C* **2009**, *113*, 4768−4778.
(50) Zhong, D. K.; Sun, J.; Inumaru, H.; Gamelin, D. R. Solar Water Oxidation by Composite Catalyst/α-Fe_2O_3 Photoanodes. *J. Am. Chem. Soc.* **2009**, *131*, 6086−6087.
(51) Saremi-Yarahmadi, S.; Tahir, A. A.; Vaidhyanathan, B.; Wijayantha, K. G. U. Fabrication of Nanostructured α-Fe_2O_3 Electrodes Using Ferrocene for Solar Hydrogen Generation. *Mater. Lett.* **2009**, *63*, 523−526.
(52) Carraro, G.; Gasparotto, A.; Maccato, C.; Bontempi, E.; Bilo, F.; Peeters, D.; Sada, C.; Barreca, D. A Plasma-Assisted Approach for the Controlled Dispersion of CuO Aggregates into β Iron(III) Oxide Matrices. *CrystEngComm* **2014**, *16*, 8710−8716.
(53) Tang, J.; Durrant, J. R.; Klug, D. R. Mechanism of Photocatalytic Water Splitting in TiO_2. Reaction of Water with Photoholes, Importance of Charge Carrier Dynamics, and Evidence for Four-Hole Chemistry. *J. Am. Chem. Soc.* **2008**, *130*, 13885−13891.
(54) Tamaki, Y.; Furube, A.; Murai, M.; Hara, K.; Katoh, R.; Tachiya, M. Direct Observation of Reactive Trapped Holes in TiO_2 Undergoing Photocatalytic Oxidation of Adsorbed Alcohols: Evaluation of the Reaction Rates and Yields. *J. Am. Chem. Soc.* **2005**, *128*, 416−417.
(55) Moulder, J. F.; Stickle, W. F.; Sobol, P. E.; Bomben, K. D. *Handbook of X-ray Photoelectron Spectroscopy*; Perkin Elmer Corporation: Eden Prairie, MN, 1992.
(56) Pattern no. 33-0664, JCPDS, 2000.
(57) Carraro, G.; Maccato, C.; Bontempi, E.; Gasparotto, A.; Lebedev, O. I.; Turner, S.; Depero, L. E.; Van Tendeloo, G.; Barreca, D. Insights on Growth and Nanoscopic Investigation of Uncommon Iron Oxide Polymorphs. *Eur. J. Inorg. Chem.* **2013**, *2013*, 5454−5461.
(58) Carraro, G.; Sugrañez, R.; Maccato, C.; Gasparotto, A.; Barreca, D.; Sada, C.; Cruz-Yusta, M.; Sánchez, L. Nanostructured Iron(III) Oxides: From Design to Gas- and Liquid-Phase Photo-Catalytic Applications. *Thin Solid Films* **2014**, *564*, 121−127.
(59) Iribarren, A.; Castro-Rodríguez, R.; Sosa, V.; Peña, J. L. Band-Tail Parameter Modeling in Semiconductor Materials. *Phys. Rev. B* **1998**, *58*, 1907−1911.
(60) Iribarren, A.; Castro-Rodríguez, R.; Sosa, V.; Peña, J. L. Modeling of the Disorder Contribution to the Band-Tail Parameter in Semiconductor Materials. *Phys. Rev. B* **1999**, *60*, 4758−4762.

DOI: 10.1021/acsami.5b00919
ACS Appl. Mater. Interfaces 2015, 7, 8667−8676